Effects of topological boundary conditions on Bell nonlocality

Patrick Emonts , ^{1,*} Mengyao Hu , ^{1,*} Albert Aloy , ^{2,3} and Jordi Tura ¹ Instituut-Lorentz, Universiteit Leiden, P.O. Box 9506, 2300 RA Leiden, The Netherlands

²Institute for Quantum Optics and Quantum Information, Austrian Academy of Sciences, Boltzmanngasse 3, A-1090 Vienna, Austria ³Vienna Center for Quantum Science and Technology, Faculty of Physics, University of Vienna, Boltzmanngasse 5, A-1090 Vienna, Austria



(Received 14 June 2024; accepted 2 August 2024; published 3 September 2024)

Bell nonlocality is the resource that enables device-independent quantum information processing tasks. It is revealed through the violation of so-called Bell inequalities, indicating that the observed correlations cannot be reproduced by any local hidden-variable model. While well explored in few-body settings, the question of which Bell inequalities are best suited for a given task remains quite open in the many-body scenario. One natural approach is to assign Bell inequalities to physical Hamiltonians, mapping their interaction graph to two-body, nearest-neighbor terms. Here, we investigate the effect of boundary conditions in a two-dimensional square lattice, which can induce different topologies in lattice systems. We find a relation between the induced topology and the Bell inequality's effectiveness in revealing nonlocal correlations. By using a combination of tropical algebra and tensor networks, we quantify their detection capacity for nonlocality. Our work can act as a guide to certify Bell nonlocality in many-qubit devices by choosing a suitable Hamiltonian and measuring its ground-state energy, a task that many quantum experiments are purposely built for.

DOI: 10.1103/PhysRevA.110.032201

I. INTRODUCTION

Nonlocality is a fundamental characteristic of Nature in which the statistics obtained by taking certain local measurements on some composite (quantum) systems cannot be replicated by any local hidden-variable model [1]. No local deterministic strategy, even if aided by shared randomness, can replicate these so-called nonlocal correlations [2]. The violation of a Bell inequality witnesses the presence of nonlocality [3], and it has recently been proven in several loophole-free Bell experiments [4-8]. Nonlocal correlations allow one to detect entanglement from a minimal set of assumptions, under the so-called device-independent (DI) paradigm. Nonlocality is the resource underpinning the implementation of DI quantum information protocols (DIQIPs) such as DI quantum key distribution [9,10], DI randomness amplification [11,12], or DI self-testing [13]. In the multipartite scenario, however, a thorough understanding of the emergence of nonlocal correlations remains elusive.

Motivated by the advent of DIQIPs, designing operationally useful Bell inequalities has been a topic of intensive research in recent years. To distinguish classical from non-local correlations, it is convenient to study correlations in terms of local hidden-variable models (LHVMs). The correlations of LHVMs can be characterized by a polytope. The characterization of the LHVM polytope gives a geometrically complete and minimal description of the LHVM set in terms of the so-called facets [14], or tight Bell inequalities. However, these quickly lose the properties that make them appealing for DIQIP tasks, even as the parameters of the Bell scenario only slightly increase. For instance, the

Clauser-Horne-Shimony-Holt (CHSH) inequality [15] is tight and self-tests the maximally entangled state of two qubits, but its facet generalization to more outcomes, such as the Collins-Gisin-Linden-Massar-Popescu (CGLMP) inequality [16], loses that property and needs to be tilted [17]. Therefore, even the computationally prohibitive method of finding all facet Bell inequalities is no guarantee to yield a useful result. Roughly speaking, the underlying reason may be that there is nothing quantum in the definition of a LHV model.

In the multipartite case, the complexity of finding all facets would scale as $O\{\exp[\exp(n)]\}$ for n parties, so radically different techniques are necessary [18]. Restricting the study to those Bell inequalities that consist of few-body correlators and inherit the geometry of the problem is a good trade-off between complexity and representability, further allowing for the experimental implementation of Bell correlation witnesses [19–21]. There, one can establish a natural connection to local Hamiltonians, looking at their ground-state energy to witness nonlocality. However, this is not a one-to-one correspondence: a Bell inequality may be associated to many Hamiltonians, and a Hamiltonian may act as a particular Bell operator of many inequalities. Here, a Bell operator corresponds to the quantum operator resulting from a choice of measurements for a given Bell inequality.

The question of optimal constituents of a good Bell inequality for multipartite correlations is rather open-ended, typically involving multiple optimizations. We know that a certain degree of frustration must be present among the correlators: e.g., the minus sign in the CHSH inequality $\langle A_0B_0\rangle + \langle A_0B_1\rangle + \langle A_1B_0\rangle - \langle A_1B_1\rangle \leqslant \beta$ guarantees that the LHVM (classical) bound, $\beta_c=2$, is strictly smaller than the algebraic bound, $\beta_{\rm alg}=4$ [3]. Otherwise, we get a completely trivial inequality. As a straightforward generalization, one might consider a multipartite system on a one-dimensional lattice. On every site, one might replicate a O(1)-partite

^{*}These authors contributed equally to this work.

inequality, such as the CHSH, with, e.g., alternating weights depending on some coupling parameter, thus creating a multipartite inequality [22], which can be seen as a dimer covering of the one-dimensional (1D) lattice. In contrast, with a homogeneous choice, one replicates the case of translationally invariant inequalities with O(1)-nearest-neighbor interactions, a method that has allowed one to characterize infinite, translationally invariant inequalities in 1D for some scenarios [23].

In one spatial dimension, the number of possibilities is rather limited: one can only place dimers in the, e.g., even-odd links and only has the choice of open vs periodic boundary conditions and desirable properties due to finite-size effects that wash out in the thermodynamic limit [24].

In 2D lattices, the number of possibilities vastly increases, but so does the computational complexity. The number of dimer coverings increases exponentially with the number of sites and the possibilities for boundary conditions also multiply, yielding different underlying topologies, which can be classified through the fundamental theorem of compact surfaces. Hence, one should expect that the particular arrangement of the dimer covering may affect the robustness of the resulting multipartite inequality. We show that this is indeed the case and identify qualitatively and quantitatively in which way this happens for 3×3 , 4×4 , and 5×5 square lattices and boundary conditions corresponding to a torus and a Klein bottle.

In this work, we propose a method to gain insights into the interplay between frustration, boundary conditions, and finite-size effects for nonlocality detection. We therefore focus our study on square 2D lattices. Due to the immense number of free parameters in such a problem, we restrict ourselves to a CHSH inequality in every link, with mutually unbiased measurements at every site. We build the multipartite Bell inequality through a dimerization procedure: By picking a dimer covering of the lattice, we place a higher weight on the links with a dimer. The resulting Bell operator can be straightforwardly interpreted as a local Hamiltonian. We compute the classical bound and quantum value of the Bell operator with a combination of tropical algebra and tensor network methods [25].

We find that the sole arrangement of dimers has a pronounced effect on the capacity of the Bell inequality to detect nonlocal correlations. We compute the detection capacity of individual inequalities by comparing their classical bound and their quantum value. The detection capacity for small systems shows clear differences depending on the boundary conditions of the system. By analyzing the robustness of the inequality to noise on the coupling parameter, we suggest the most robust configurations for on-device testing.

The rest of this paper is organized as follows: In Secs. II and III, we give an introduction to Bell inequalities and how they are connected to Hamiltonians. Section IV explains the methods to obtain and analyze the two-dimensional models. The results are presented in Sec. V. Finally, we conclude and present an outlook in Sec. VI.

II. PRELIMINARIES—BELL INEQUALITIES

The traditional scenario to observe nonlocality is two distant parties, Alice and Bob, who can perform measurements on a shared physical system. Each of them chooses among m different measurements and each measurement can yield d possible outcomes. Here, we will directly start with N parties sharing a physical system since we are interested in many-body nonlocality. We denote the measurement choices of all parties with $x_i \in [m] = \{0, \ldots, m-1\}$ and their respective outputs $a_i \in [d] = \{0, \ldots, d-1\}$ for $i \in [N] = \{0, \ldots, N-1\}$, respectively. In general, the correlations between results obtained in the above process are governed by the conditional probability distribution $P(\mathbf{a}|\mathbf{x}) := P(a_0, \ldots, a_{N-1}|x_0, \ldots, x_{N-1})$ with $\mathbf{a} := a_0, \ldots, a_{N-1}$ and $\mathbf{x} := x_0, \ldots, x_{N-1}$. This joint probability distribution is fully described by the $(md)^N$ dimensional vector

$${P(a_0,\ldots,a_{N-1}|x_0,\ldots,x_{N-1})}_{\mathbf{a};\mathbf{x}}.$$
 (1)

All entries satisfy the m^N affine-linear equations,

$$\sum_{a} P(a_0, \dots, a_{N-1} | x_0, \dots, x_{N-1}) = 1, \ \forall \mathbf{x},$$
 (2)

to be normalized as well as the inequalities $P(\mathbf{a}|\mathbf{x}) \ge 0$ to be non-negative.

The nonsignaling principle [26,27] (all parties are spatially separated and cannot communicate instantaneously) leads to well-defined marginals, i.e., the marginals observed by any subset of parties do not depend on the choices of measurements performed by the rest. That is, for all x_i , x'_i ,

$$\sum_{a_i} P(a_0, \dots, a_i, \dots, a_{N-1} | x_0, \dots, x_i, \dots, x_{N-1})$$

$$= \sum_{a_i} P(a_0, \dots, a_i, \dots, a_{N-1} | x_0, \dots, x_i', \dots, x_{N-1}). (3)$$

Thus, $P(a_{i_1}, \ldots, a_{i_l} | x_{i_1}, \ldots, x_{i_l})$ is well defined on any subset $\{i_1, \ldots, i_l\} \subseteq [N]$.

To detect nonlocality, the goal is to find Bell inequalities separating the polytope $\mathcal L$ of local correlations described by LHVM from the convex set of quantum correlations. LHVM can be formulated as

$$P(\mathbf{a}|\mathbf{x}) = \sum_{\lambda} p(\lambda) \prod_{i=0}^{N-1} P(a_i|x_i, \lambda), \tag{4}$$

where λ is some hidden variable. Among LHVM correlations, of special interest are local deterministic strategies (LDSs) [2], which correspond to the vertices of the LHVM polytope and factorize as

$$P(a_0, \dots, a_{N-1} | x_0, \dots, x_{N-1}) = \prod_{i=0}^{N-1} P(a_i | x_i),$$
 (5)

where $P(a_i|x_i)$ are deterministic functions.

In contrast, the quantum correlations are given by Born's rule:

$$P(a_0, \dots, a_{N-1} | x_0, \dots, x_{N-1})$$

$$= \text{Tr} \left[\rho_N \left(\mathcal{M}_{0, x_0}^{a_0} \otimes \dots \otimes \mathcal{M}_{N-1, x_{N-1}}^{a_{N-1}} \right) \right], \tag{6}$$

where ρ_N is an N-partite quantum state and $\mathcal{M}_{i,x_i}^{a_i} \geq 0$ is the x_i th measurement with outcome a_i performed by party A_i , satisfying the normalization condition $\sum_{a_i} \mathcal{M}_{i,x_i}^{a_i} = \mathbb{I}$. The convex set of such quantum correlations is denoted by \mathcal{Q} .

Tight Bell inequalities are facets of the local polytope \mathcal{L} separating local correlations from quantum correlations. These inequalities take the form $\mathcal{I}_{N,m,d} \geqslant \beta_C$, where

$$\mathcal{I}_{N,m,d} := \sum_{\mathbf{a},\mathbf{x}} \alpha_{\mathbf{a},\mathbf{x}} P(\mathbf{a}|\mathbf{x}), \tag{7}$$

and $\alpha_{\mathbf{a},\mathbf{x}} \in \mathbb{R}$ are some coefficients and $\beta_C = \min_{P(\mathbf{a}|\mathbf{x}) \in \mathcal{L}} I_{N,m,d}$ is the classical bound of the Bell inequality. Note that depending on the underlying physical model, a given set of correlations might or might not be compatible with it. For instance, if the model is LHVM, $\mathcal{I}_{N,m,d}$ is lower bounded by β_C . Similarly, if we consider quantum theory as the underlying physical model, the inequality $\mathcal{I}_{N,m,d} \geqslant \beta_Q$, where $\beta_Q = \inf_{P(\mathbf{a}|\mathbf{x}) \in \mathcal{Q}} I_{N,m,d}$, probes the limits of the quantum set \mathcal{Q} . It is often referred to as the quantum Bell inequality, with β_Q representing the associated quantum bound or Tsirelson bound [26].

Naturally, it is desirable to have a maximal distance between β_C and β_Q to facilitate the detection of Bell nonlocality in experiments. We can compute the classical bound of $\mathcal{I}_{N,m,d}$ by minimizing it over all the LDSs of N parties. An LDS of a single party can be described by a map $\phi_s : [m] \mapsto [d]$ that deterministically associates an outcome to every input. We can enumerate all d^m possible strategies as the set of LDSs, $S_{LDS} := [d^m]$. In the case of the CHSH inequality with m = 2measurements and d = 2 (binary) outcomes, the set of LDSs is $S_{LDS} = \{0, ..., 3\}$. The input-output maps are $\phi_0(x) = 0$, $\phi_1(x) = x$, $\phi_2(x) = 1 - x$, and $\phi_3(x) = 1$. In other words, the strategies are equivalent to always choosing 0, choosing the input, choosing the opposite of the input, or always choosing 1, respectively. Now the probability distribution of a single party associated with the LDS $s \in S_{LDS}$ is given by the Kronecker delta, $P_s(a|x) := \delta[a - \phi_s(x)]$. For an *N*-partite strategy vector $s \in S_{\text{LDS}}^N$, the joint probability distribution of LDS can then be written as $P_s(a_0, \ldots, a_{N-1} | x_0, \ldots, x_{N-1}) :=$ $\prod_{i=0}^{N-1} P_{s_i}(a_i|x_i)$. Thus, Eq. (7) can be rephrased as

$$\mathcal{I}_{N,m,d}(\mathbf{s}) := \sum_{\mathbf{a},\mathbf{x}} \alpha_{\mathbf{a},\mathbf{x}} P_{\mathbf{s}}(\mathbf{a}|\mathbf{x}), \tag{8}$$

where $\mathbf{s} \in \mathcal{S}_{\text{LDS}}^{N}$ is an N-partite strategy vector, and the classical bound

$$\beta_C = \min_{P(\mathbf{a}|\mathbf{x}) \in \mathcal{L}} I_{N,m,d} = \min_{\mathbf{s} \in \mathcal{S}_{\text{IDS}}^N} \mathcal{I}_{N,m,d}(\mathbf{s}). \tag{9}$$

We will use this expression to compute the classical bound in Sec. IV B.

III. THE MODEL

The relationship between Bell inequalities and Hamiltonians provides a way to test nonlocality and design quantum systems to demonstrate nonlocal correlations [19,22,23,28–33]. For a given Bell inequality, one can construct a Hamiltonian coinciding with its Bell operator, which provides a way to optimize the many-body system to exhibit nonlocal correlations. If the ground-state energy of the Hamiltonian is smaller than the classical bound given by the Bell inequality, it certifies that the quantum system exhibits nonlocal correlations. Conversely, we can also associate a Bell inequality to a given spin Hamiltonian such that its Bell operator coincides

2D systems

FIG. 1. Dimer configurations in one and two dimensions with periodic boundary conditions. In the one-dimensional case, there are only two distinct dimer coverings (links on even or odd links). In two spatial dimensions, multiple dimer configurations are possible. Dimer configurations related by spatial symmetries (see gray box) yield the quantum and classical bounds.

with it. This correspondence is not one to one; for details, see Appendix A.

One example for a many-body inequality is the CHSH Bell expression realized on every link of a 1D system. On a chain with N qubits (N even), one can construct a 1D Bell inequality, $I^{(N)}(\epsilon) = \sum_{i=0}^{N-1} f_i(\epsilon) \mathcal{I}^{(i,i+1)}$, where $\mathcal{I}^{(i,i+1)}$ is the CHSH inequality between sites i and i+1, and $f_i(\epsilon)$ are real coefficients of the multipartite inequality. The Hamiltonian

$$H = \sum_{i=0}^{N-1} f_i(\epsilon) \left(\sigma_x^{(i)} \sigma_x^{(i+1)} + \sigma_x^{(i)} \sigma_z^{(i+1)} + \sigma_z^{(i)} \sigma_x^{(i+1)} - \sigma_z^{(i)} \sigma_z^{(i+1)} \right)$$

$$(10)$$

with $f_i(\epsilon) = 1 + (-1)^i \epsilon$ is a special case of the multipartite Bell inequality $I^{(N)}(\epsilon)$, which we choose in this work. For ease of description and fair comparison between different systems, we choose a version of the CHSH Bell operator with equal measurements at all sites throughout this work [22], i.e., $A_0 = B_0 = \sigma_x$ and $A_1 = B_1 = \sigma_z$. Thus, Eq. (10) is equivalent to a weighted CHSH expression on each link. To obtain a Bell violation with identical measurements for both parties, we use a rotated Bell state, $|\phi\rangle = \frac{1}{\sqrt{2}}(|00\rangle + e^{\pi i/4}|11\rangle)$. The structure of the coefficients $f_i(\epsilon)$ follows a dimer pattern: every second link has a strong coupling, and the others are only weakly coupled (cf. Fig. 1). This construction has two interesting limiting cases: $\epsilon = 0$ and $\epsilon = 1$. For $\epsilon = 0$, the multipartite Bell inequality $I(\epsilon)$ corresponds to a sum of CHSH inequalities with the same weights between all the neighboring nodes: $I(0) = \sum_{i=0}^{N-1} \mathcal{I}^{(i,i+1)}$. The inequality I(0) cannot be violated due to the monogamy of Bell correlations [34,35], which implies that the violation of CHSH inequality between nodes i and i + 1 prohibits any violation of other CHSH inequalities involving nodes connected to nodes i and i + 1.

In the other limiting case $\epsilon=1$, the Bell inequality $I(\epsilon)$ corresponds to a sum of disjoint CHSH inequalities on all links emanating from an even node. The expression $I(1)=2\sum_i \mathcal{I}^{(i,i+1)}$ is maximally violated by the state $\bigotimes_i |\phi_2\rangle_{i,i+1}$,

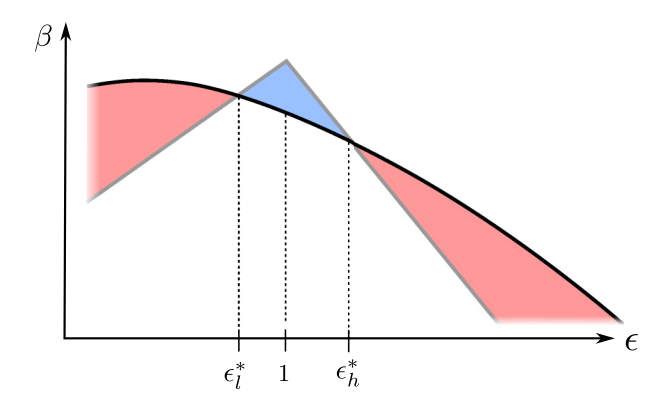


FIG. 2. Possible violation of a Bell inequality. Depending on ϵ , the classical bound β_C (gray line) and the quantum value β_Q (black line) of the inequality vary. The region where a violation is possible (in blue) depends on the size of the system, the dimer configuration, and the boundary conditions. The intersections between the classical bound and the quantum value are the critical values of the coupling ϵ_I^* and ϵ_h^* .

where $|\phi_2\rangle = \frac{1}{\sqrt{2}}(|00\rangle + e^{\pi i/4}|11\rangle)$, and the index *i* only iterates over even sites. Moreover, the inequality is maximally violated with a quantum value of $-N\sqrt{2}$.

While we know the point of maximal violation at $\epsilon = 1$, the range of the couplings ϵ with a possible violation is not known. In one dimension, the classical bound $\beta_C(\epsilon)$ of $I^{(N)}(\epsilon)$ can be obtained by contracting a tropical tensor network; for details, see Sec. IV B. Finding the quantum value $\beta_O(\epsilon)$ can be reduced to finding the ground-state energy of the Hamiltonian H in Eq. (10). Here, we are careful to call the ground state of the Hamiltonian the quantum value since we keep a fixed set of measurements during the minimization. The quantum bound is the infimum over all measurements and states in the quantum set. The nonlocality is detected when $\beta_O(\epsilon) < \beta_C(\epsilon)$. As discussed in Ref. [22], the dimer model allows for violations of Bell inequalities in a region around $\epsilon = 1$, where $\epsilon = 1$ corresponds to one of the limiting cases discussed above. Figure 2 shows the behavior in a sketch. A violation of the Bell inequality can only be detected inside of the blue-shaded region. The boundaries of the region in terms of ϵ are given by the intersections of the quantum value and the classical bound,

$$\beta_O(\epsilon^*)/\beta_C(\epsilon^*) = 1.$$
 (11)

We denote these values of the coupling ϵ^* on either side of $\epsilon = 1$ by ϵ_l^* and ϵ_h^* , respectively.

In a single spatial dimension, the choice of inequalities is heavily restricted by the limited choice of boundary conditions and dimer configurations. In 1D, there are only two boundary conditions: open or periodic boundary conditions. Additionally, the weighted links can either be on the odd or on the even links, leading to only four possibilities in total.

The variety of inequalities changes dramatically in two spatial dimensions. Instead of the two possible dimer coverings as in one dimension, the number of allowed dimer coverings scales exponentially with system size in two dimensions (cf. Fig. 1). Additionally, different boundary conditions are possible. According to the classification theorem for

compact, connected surfaces, every compact connected surface is homeomorphic to the connected sum of torus, Klein bottle, and sphere [36]. We limit our study to the topologies of torus and Klein bottle since the sphere is not well suited for a square lattice.

The inequality of the 1D case can be readily generalized to the two-dimensional case. Instead of a fixed link pattern (stronger weights on the even links) as in the one-dimensional case, we choose a fixed dimer covering on the square lattice and place the weighted links on the dimers. Thus one can construct the multipartite Bell expression for a given dimer configuration,

$$I(\epsilon) := \sum_{\langle i,j \rangle} f_{i,j} \cdot \mathcal{I}^{(i,j)}, \tag{12}$$

where

$$f_{i,j}(\epsilon) = \begin{cases} 1 + \epsilon & \text{if } (i,j) \text{ in dimer} \\ 1 - \epsilon & \text{if } (i,j) \text{ not in dimer,} \end{cases}$$
 (13)

and $\langle i, j \rangle$ indicates that nodes i and j are nearest neighbors. The two limiting cases of this construction are the same as the limiting cases of the 1D construction. Following the same strategy as in the one-dimensional case, we construct the corresponding Hamiltonian,

$$H := \sum_{\langle i,j \rangle} f_{i,j}(\epsilon) \left(\sigma_x^{(i)} \sigma_x^{(j)} + \sigma_x^{(i)} \sigma_z^{(j)} + \sigma_z^{(i)} \sigma_x^{(j)} - \sigma_z^{(i)} \sigma_z^{(j)} \right),$$
(14)

where $f_{i,j}(\epsilon)$ is defined as in Eq. (13).

To detect nonlocality, we are again interested in cases where the Bell expression has a quantum value β_Q and a classical bound β_C such that $\beta_Q(\epsilon) < \beta_C(\epsilon)$. The size and shape of the region with a violation depends on the chosen dimer configuration, the size of the system, and the boundary conditions. The larger the distance between ϵ_h^* and ϵ_l^* , the higher the capacity of the inequality to detect nonlocality. The goal is to find a combination of dimer configuration and boundary condition where the interval with a violation is maximal. These configurations are prime candidates for experimental realization to certify nonlocality.

IV. METHODS

To maximize the size of the violating region, we first need a way to compute the two bounds of the violating region ϵ_l^* and ϵ_h^* . If it does not matter whether we treat the lower or upper bound, we will refer to both of them jointly with ϵ^* . The algorithm to estimate the critical values of epsilon proceeds in two major steps. First, we address the dependence of the dimer configuration. All dimer coverings can be classified with regard to the symmetries of the lattice.

A simple example of equivalent dimer coverings is two patterns that are rotated by 90 degrees on a lattice with periodic boundary conditions. These two coverings will give the same values for ϵ^* and we only have to compute them once. We explore the symmetries of the lattices in Sec. IV A.

The second step is the search for the actual value of ϵ^* . Since ϵ^* is a quotient of a classical bound and a quantum value, we have to compute both of them. By iteratively com-

puting the classical (cf. Sec. IV B) and the quantum value(cf. Sec. IV C), we can find the intersection between the two bounds in terms of ϵ , the critical value ϵ^* (cf. Sec. IV D).

A. Classification of dimer coverings

Let us start with the dimer coverings. In one dimension, as considered in [22], there are only two different dimer coverings. The dimers can be on even or on odd links (cf. Fig. 1).

In two dimensions, the number of possible dimer configurations scales with the size of the lattice. Since we are interested in maximal violations, we focus on maximal dimer coverings. A maximal dimer covering distributes as many dimers on a given lattice as is allowed.

However, not all maximal dimer coverings are independent. If two dimer coverings are connected by a symmetry U that commutes with the Hamiltonian [U, H] = 0, the quantum value will not be affected. The unitaries U are generated by lattice symmetries O like rotations or mirroring (cf. Fig. 1).

As an example, we will consider the symmetries of the torus. In total, the torus has five nondecomposable symmetries O: right shift, up shift, rotation by 90 degrees, horizontal mirror, vertical mirror. Details about the symmetry considerations and the symmetries of the Klein bottle are given in Appendix B. For concreteness, we focus on a specific symmetry, the right shift O_{rs} (right shift). The operation right shift is a bijection O_{rs} from the set $\mathbb{S}_{n,T}$ to the set $\mathbb{S}_{n,T}$, where $\mathbb{S}_{n,T}$ is the set of all maximal dimer coverings on a square lattice of size $n \times n$ with periodic boundary conditions. The bijection O_{rs} can be written as follows:

$$O_{rs}: \mathbb{S}_{n,T} \to \mathbb{S}_{n,T},$$

$$S_T := (\mathbf{a}_0, \mathbf{a}_1, \dots, \mathbf{a}_{n-1}) \mapsto (\mathbf{a}_1, \dots, \mathbf{a}_{n-1}, \mathbf{a}_0), \quad (15)$$

where $\mathbf{a}_0, \dots, \mathbf{a}_{n-1}$ are the *n* columns with *n* sites each of the square lattice.

We can use the symmetry structure of the generators now to reduce the number of dimer coverings that we have to consider. The generators of the symmetries form a group. Their action can be faithfully represented by the action of the group elements as in Eq. (15). Each unique class of dimer configurations is given by one of the orbits of the group action applied to the set of dimer coverings. Since the symmetries commute with the Hamiltonian, ϵ^* is identical in each orbit. Thus, it is sufficient to compute ϵ^* for one representative from each orbit. In the following, we will call the different orbits a *class* of dimer coverings. In Sec. IV D, the equivalence of different dimer coverings in the same class is used to benchmark the algorithm. Further details on the group structure can be found in Appendix B.

In practice, the group orbits are obtained by a graph-exploration algorithm through a pregenerated list of all maximal dimer coverings. Here, we pick depth-first search (DFS) for ease of implementation. This list is obtained with a backtracking procedure. The idea of the backtracking algorithm is to explore all valid configurations of maximal dimer coverings in a structured way. The algorithm places the dimers successively on the lattice while checking for contradictions with the dimer constraint. If a contradiction is found, all further attempts are stopped (i.e., this branch of the recursive

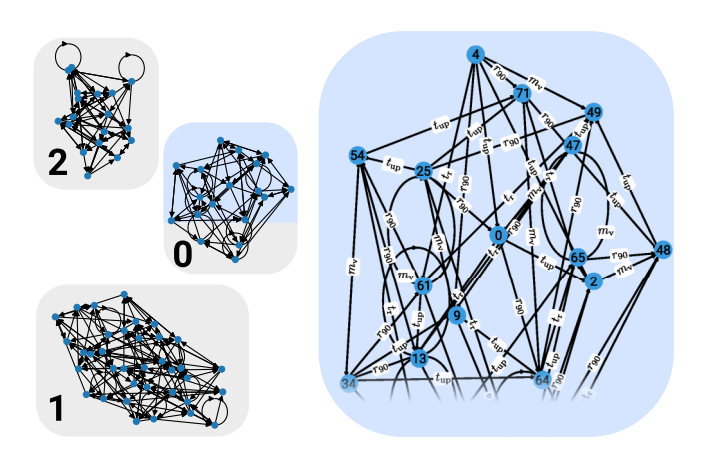


FIG. 3. Graph orbits of a 3×3 torus. The dimers form three distinct classes, visible as three connected subgraphs. Each vertex corresponds to one dimer covering. The labels on the edges represent the symmetry operations that connect the different coverings. The shaded region in blue is a zoomed-in version of class 0.

search is discarded) and the algorithm continues from the last valid configuration with another placement strategy.

Given the list of maximal dimer coverings, we can classify them. Starting from the first dimer covering, we recursively apply the generators of the symmetry group. At each level of the recursion, we first apply a new operation before exploring other paths (following the depth-first strategy). By tracking the already visited configurations, we discover a given orbit of the group action since we cannot leave the starting configuration's orbit by applying only symmetry operations. After exploring the full orbit, we pick a new dimer covering that has not been visited before. It must belong to a different orbit (class). The procedure ends when all dimer coverings in the list have been visited. For further details on the algorithm, see Appendix C.

As an example, we consider a square lattice of 3×3 sites on the torus. Figure 3 shows the three classes of dimer coverings as discovered with DFS. Each vertex of the graph corresponds to one maximal dimer covering. They are connected by directed edges labeled with the operation that connects the two. Instead of computing ϵ^* for all 72 dimer coverings, we can compute the value for only three classes.

An additional benefit of the DFS is an implicit check of the backtracking procedure. The backtracking procedure places dimers on the lattice without any awareness of the symmetries. The DFS applies all symmetry generators to all known dimer coverings. During the DFS, we only find known dimer coverings during the DFS algorithm, a necessary condition for the correctness of the backtracking algorithm.

B. Computing the classical bound

After reducing the number of dimer coverings, we turn our attention to the computation of ϵ^* ; cf. Eq. (11). We start by computing the classical bound β_C . Its computation is equivalent to finding the optimal set of LDSs for each party. This assignment of local strategies minimizes the classical bound β_C of the Bell inequality.

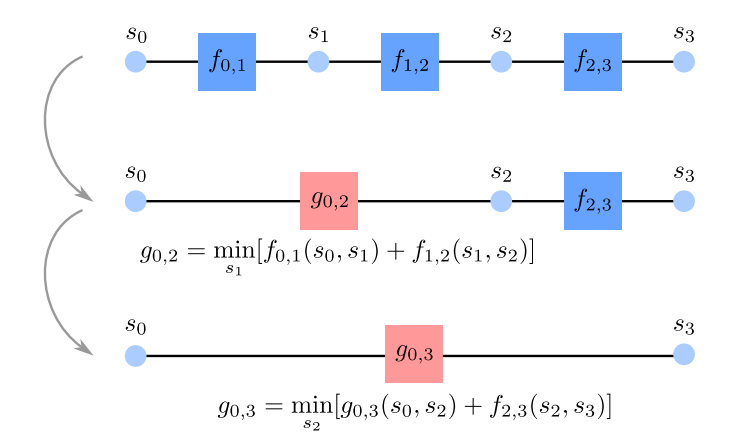


FIG. 4. Example of successive contractions in one dimension. In each step, one variable is eliminated by minimizing over it.

The number of LDSs in a system of N parties grows exponentially with N as $(md)^N$. Thus, solving the problem by fully enumerating all possible combinations quickly becomes prohibitively expensive. For small systems, e.g., nine sites, the number of LDSs is $4^9 = 262144$, which is still manageable. Already at system sizes of 4×4 , a more sophisticated approach is needed.

1. Tropical tensor networks

Tropical tensor networks are a more efficient way to obtain results for discrete optimization problems, e.g., the ground state of classical spin systems [37] or classical bounds of Bell inequalities [25]. As the name suggests, we need two main ingredients: tropical algebra [38] and tensor networks [39].

Tropical algebra is defined on the tropical semiring ($\mathbb{R} \cup \{+\infty\}, \oplus, \odot$), where the tropical addition \oplus and tropical multiplication \odot are defined as

$$x \oplus y = \min\{x, y\}, \quad x \odot y = x + y. \tag{16}$$

This min-plus algebra yields a natural framework to formulate optimization problems [40], e.g., the optimization of the classical bound β_C . A typical example of a graph optimization problem is given in Appendix D.

In the framework of tropical tensor networks, it is possible to interpret functions with a finite number of possible inputs as tensors. The functions $f(s_i, s_{i+1})$ describing the Bell inequality in the classical bound accept only d discrete inputs, corresponding to the number of local deterministic strategies. To simplify, let us start by restricting to 1D lattices. In particular, let us denote the N nodes of a chain as $i \in [N]$ and the strategy of each node is s_i .

Then, as defined in Eq. (8), a Bell inequality involving, at most, nearest-neighbor interactions will be a linear combination of functions $f_{i,i+1} := f(s_i, s_{i+1})$ (see Fig. 4) such that

$$\sum_{i=0}^{\tilde{N}} f(s_i, s_{i+1}) - \beta_C \geqslant 0, \tag{17}$$

and the classical bound is

$$\beta_C := \min_{\mathbf{s} \in \mathcal{S}_{\text{LDS}}^{\tilde{N}}} \sum_{i=0}^{\tilde{N}} f(s_i, s_{i+1}). \tag{18}$$

Notice that we use $\tilde{N} = N - 2$ for open boundary conditions or $\tilde{N} = N - 1$ for periodic boundary conditions, respectively.

The form of Eq. (18) is a formulation amenable to tropical tensor network contractions, significantly increasing the performance to obtain β_C . The idea here is to optimize one strategy s_i at a time, instead of all strategies s at once. This can be achieved by introducing a function,

$$g_{i,i+2} := \min_{s_{i+1}} \left[f_{i,i+1}(s_i, s_{i+1}) + f_{i+1,i+2}(s_{i+1}, s_{i+2}) \right], \quad (19)$$

which optimizes over the strategy s_{i+1} and effectively removes it, as illustrated in Fig. 4. By iterating the function $g_{i,i+2}$ for the remaining nodes, a situation with only two remaining nodes is reached. At this point, one can efficiently obtain the final optimal value β_C .

To complete the mapping from function minimization to tensor networks, we express the functions over discrete sets as tensors. In the case of CHSH, d = 2 and f can be fully described by a 4×4 matrix F. Thus, the minimization over a party [cf. Eq. (19)] can be written as

$$G = F \odot F, \tag{20}$$

where the matrix G corresponds to the new function $g(s_i, s_{i+2})$ in Eq. (19) and \odot stands for tropical matrix multiplication. Adhering to standard tensor network notation, we can write the full dynamic programming approach including the iteration over all sites as a contraction:

Here, the tensors s_i are δ distributions which are inserted for increased similarity with Fig. 4. Leaving them out does not change the expression. For further details on tropical tensor networks, we refer to Ref. [25].

2. Grouping by columns

Let us now consider 2D lattices. The procedure to obtain β_C follows the same guidelines presented in the previous section, but this time we are going to group the nodes by columns. The exact contraction of 2D tensor networks scales exponentially with system size [41]. In contrast to a one-dimensional lattice, the path during the iteration of $g_{i,i+2}$ is ambiguous. Thus, we reduce the two-dimensional case to the one-dimensional case by grouping columns of the lattice. This procedure exponentially increases the number of strategies per site. It does not solve the issue of exponential scaling, but only confines it to one spatial direction. In principle, we could investigate rectangular systems of limited height and large width. Since we are considering square systems in this work to obtain a fair comparison between different sizes, the algorithm will only work for moderately sized lattices.

To group the columns, we label the nodes (i, j) with strategy s_{ij} and i, j corresponding to the row and column, respectively; this time we introduce a function $g_{\text{col } j, \text{col } j+1} := g(\mathbf{s}_j, \mathbf{s}_{j+1})$, where \mathbf{s}_j is the tuple of all the variables $s_{i,j}$ in the jth column. Now, in each contraction step, we are going to

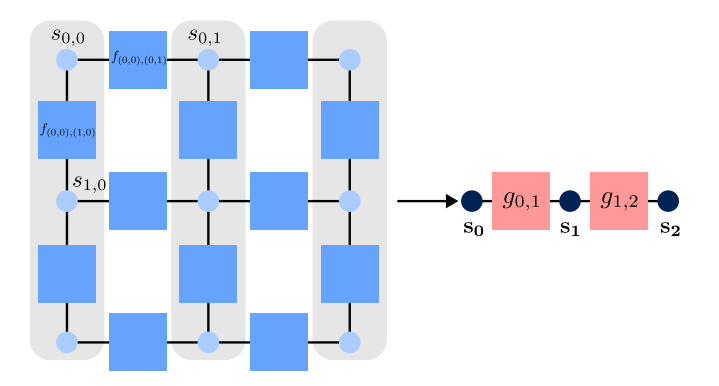


FIG. 5. The two-dimensional system can be transformed into a one-dimensional system by blocking the columns to enlarged sites. The dimension of the variables \mathbf{s}_i is exponentially bigger than the original variables s_i .

implicitly optimize over all the nodes of one column in the following manner:

$$g_{\text{col } j, \text{col } j+2} = \min_{\mathbf{s}_{j+1}} \left[\sum_{i} \underbrace{f(s_{i,j}, s_{i,j+1}) + f(s_{i,j+1}, s_{i,j+2})}_{\text{Crossed columns interactions}} + \sum_{k=0}^{2} \underbrace{\sum_{i} f(s_{i,j+k}, s_{i+1,j+k})}_{\text{Literation scheme}} \right], \tag{22}$$

where $\mathbf{s}_{j+1} = s_{0,j+1}, \ldots, s_{i,j+1}, \ldots$ are all the strategies of nodes in the j+1 column.

Let us take Fig. 5 for an explicit example. In this case, one step in the contraction, for instance, would carry on the following optimization:

$$g_{0,2} = \min_{s_{0,1}, s_{1,1}, s_{2,1}} \sum_{i=0}^{2} [f(s_{i,0}, s_{i,1}) + f(s_{i,1}, s_{i,2}) + \sum_{k=0}^{2} f(s_{i,0+k}, s_{i+1,0+k})].$$
(23)

By grouping the sites in column j into one variable \mathbf{s}_j , the optimization function $g_{0,2}$ then can be written as $g_{0,2}(\mathbf{s}_0, \mathbf{s}_2) = \min_{\mathbf{s}_1} g(\mathbf{s}_0, \mathbf{s}_1) + g(\mathbf{s}_1, \mathbf{s}_2)$.

The approach of contracting tropical tensor networks can also be phrased in terms of dynamic programming [42,43]. The contracting in one spatial dimension is equivalent to the successive optimization steps in dynamic programming.

C. Computing the quantum value

In addition to the classical bound β_C , we need to compute β_Q , the quantum value of the Bell inequality. Due to the structure of the Bell operator, the quantum value of the system corresponds to the ground-state energy of H, the Hamiltonian associated to the Bell operator (cf. Sec. III). The problem of finding β_Q is equivalent to finding the ground-state energy of H. For small systems, we can obtain the ground state by diagonalization. For larger systems, however, this procedure becomes prohibitively expensive and we use dedicated many-body methods.

In contrast to the computation of the classical bound, we use matrix product states here as a computational tool with regular algebra. Matrix product states (MPSs) are one-dimensional tensor networks and we use them as an ansatz state in a variational optimization. Due to their entanglement structure, they target directly the ground-state sector of local, gapped Hamiltonians in one space dimension [44,45]. Using variational methods such as density matrix renormalization group (DMRG) [46], they led to a deeper analytical and numerical understanding of many-body systems in one dimension [39]. We aim to find a good approximation for the ground-state energy by minimizing,

$$E_{\min} = \min_{\alpha} \frac{\langle \psi(\alpha) | H | \psi(\alpha) \rangle}{\langle \psi(\alpha) | \psi(\alpha) \rangle}, \tag{24}$$

where α is a set of matrices parametrizing the MPS.

Here, we apply MPS to two-dimensional systems by applying a snake pattern [47]. This transforms the two-dimensional system into a one-dimensional system that we can optimize with DMRG. This strategy introduces system-sized couplings in the Hamiltonian, limiting this approach to moderate system sizes. For larger systems, genuine two-dimensional approaches such as projected entangled pair states (PEPSs) would be more appropriate. While the Hamiltonian obeys the boundary conditions demanded by the system, the MPS keeps open boundary conditions. The boundary conditions are enforced by adding the couplings between the sides explicitly. The open boundary conditions for the state are chosen due to the higher numerical efficiency. Further details about the MPS simulations are given in Appendix E.

D. Computing the critical epsilon

In the last sections, we explored different methods to compute the classical bound β_C and the quantum value β_Q . Actually, we would like to compute the critical value of the coupling such that

$$\beta_O(\epsilon^*)/\beta_C(\epsilon^*) - 1 = 0. \tag{25}$$

Due to the structure of the local polytope, we expect to find one critical value of epsilon on either side of $\epsilon = 1$.

The root-finding procedure of Eq. (25) is performed by the iterative Brent-Dekker algorithm, a hybrid root-finding algorithm combining different root-finding methods [48,49]. Given an initial value of ϵ on either side of 1, the algorithm iteratively evaluates the numerator and denominator of Eq. (25) to find the critical value of ϵ^* . Since the quantum and the classical value are evaluated repeatedly, the parameters of both strategies have to be chosen with a time aspect in mind. For more details on the numerical parameters, we refer to Appendix E.

V. RESULTS

In the last section, we explored several methods to find classical bounds, quantum values, and the critical value of ϵ . In the first step, we present benchmarks using exact methods such as diagonalization for the variational simulations with tensor networks. These benchmarks are presented in Sec. V A.

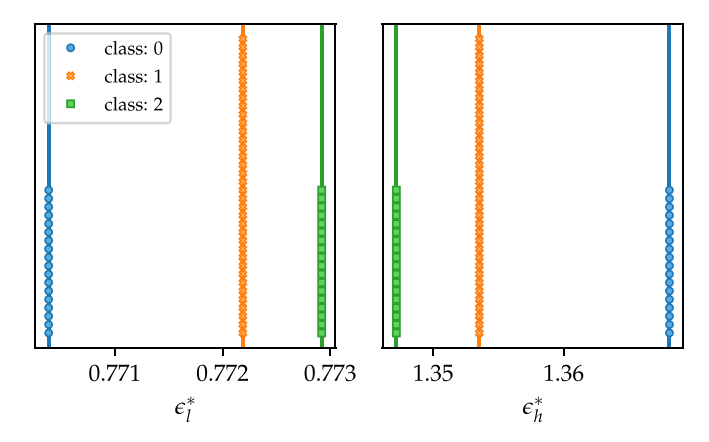


FIG. 6. Comparison of exact results (vertical lines) and MPS results (dots) for ϵ^* on a torus of size 3×3 . The left (right) panel shows value of $\epsilon_l^*(\epsilon_h^*)$ smaller (greater) than 1. Each dot represents one dimer configuration on the lattice. The vertical axis only enumerates the different dimer configurations.

Our results for the critical value of ϵ for larger systems are shown in Sec. V B.

A. Benchmark for small systems

In small systems, both the Hilbert space and the total number of dimer coverings are still small. Thus, the classical bound can be computed by enumerating all strategies and the quantum value can be evaluated by diagonalizing the Hamiltonian. The vertical lines in Fig. 6 represent the result of these exact computations. The illustration is split into two columns, i.e., one for each value ϵ^* (below and above $\epsilon=1$). The dots represent ϵ^* for each dimer covering individually. Here, the quantum value is calculated with MPSs and the classical value results from a tropical tensor network (TrTN) contraction. As expected, all points in Fig. 6 are located on the corresponding lines. Thus, the computations converged to the expected values. The plot serves as a benchmark for the variational computation since the values agree with large accuracy.

B. Critical epsilon

After checking the convergence of the algorithm, we can compute ϵ^* for larger systems. The goal is to find combinations of a dimer configuration, system size, and boundary condition that allow one to detect nonlocality over large ranges of the coupling. In the first step, we will explore the properties of the model and the violation ranges that it shows. Afterwards, concrete dimer realizations with the maximal violation will be showcased.

In total, three different system sizes are investigated, i.e., square lattices of size $n \in \{3, 4, 5\}$. Convergence for the first two lattice sizes was checked against exact diagonalization results. Figure 7 shows the minimal ϵ_l^* and maximal ϵ_h^* . The size of the violation region depends on the chosen boundary conditions. Furthermore, the size of the lattice plays a role. With increasing lattice size, the difference between both the toroidal and Klein bottle boundaries decreases. This could be expected since the bulk of the system grows faster than the boundary. Since an extensive study of a n=6 lattice exceeded our numerical resources, it is not entirely clear whether it is an effect of the lattice size or the parity of the lattice dimensions. The main problem is not the evaluation of a single model at a given coupling ϵ , but rather the large amount of classes and the repeated evaluation during the root-finding process.

For all system sizes, we observe a tendency to parallel ordering of the dimers for the lower bound of the violation interval. On the upper end, perpendicular dimers are favored. In the case of a system with n=3 on the Klein bottle, the same configuration realizes the lower and upper bounds. That makes this system a prime candidate for an experiment since the same dimer covering with different couplings will cover the whole interval.

For the two smaller system sizes, $n \in \{3, 4\}$, all dimer configurations were evaluated to guarantee convergence of the root-finding procedure. In the case of the larger lattice size, n = 5, 10 classes were evaluated for toroidal boundary conditions (see Fig. 8). Since the number of dimer configurations with Klein bottle boundary conditions exceeds 1000, we only computed one representative dimer configuration for each class.

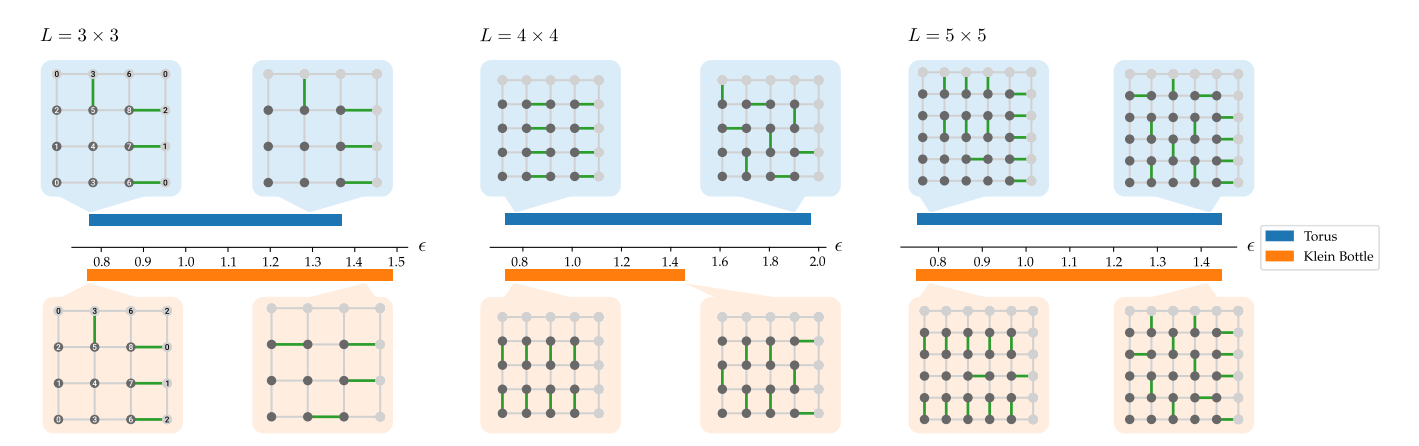


FIG. 7. Ranges of critical values for different boundary conditions and system sizes. From left to right, the three figures indicate the results for 3×3 , 4×4 , and 5×5 systems. The blue (orange) regions shows the ranges of ϵ^* for a system on a torus (Klein bottle). The bars close to the axis connect the value of the minimal and the maximal critical epsilon for a given system. The bars span across multiple classes. Insets: A dimer covering of the class with maximal (minimal) ϵ^* .

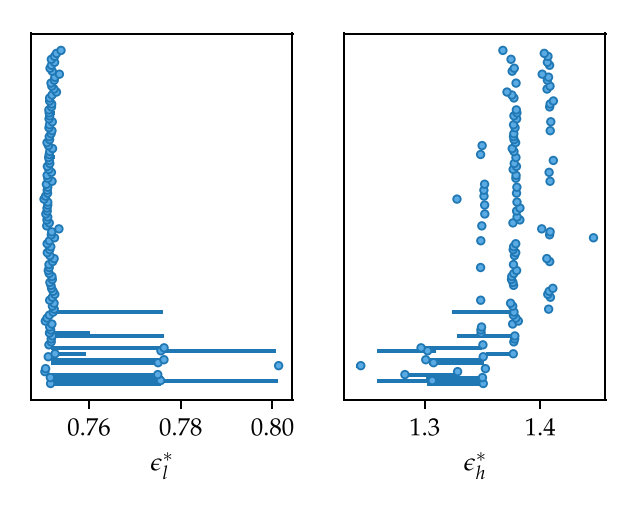


FIG. 8. Computation of ϵ^* for a 5 × 5 lattice with periodic boundary conditions. The points are the median of 10 representative dimer configurations from each class. The asymmetric error bars show the minimal and maximal deviations among all considered realizations.

For systems of size n = 5 and larger, the number of dimers exceeds the number of simulations that can be performed in a reasonable time. Instead of simulating all dimers, we will actively use the dimer classification described in Sec. IV A. Since the convergence of the MPS simulation becomes more challenging for larger systems, we simulate 10 representatives from each class. The results of the simulation are shown in Fig. 8. Note that the vertical axis in Fig. 8 does not display all dimer realizations as in Fig. 6, but the different classes. The points in the figure are the median values of the 10 simulations with different dimer coverings belonging to the same class. The asymmetric error bars represent the minimal and maximal values for the critical coupling among all runs for each class. This error measure is more pessimistic than other error measures such as the standard deviation. We choose it here to take the highly asymmetric character of the error into account. The main source of error is convergence accuracy in the MPS simulation. Since this is a variational computation, the computation always overestimates $\beta_O(\epsilon)$. Depending on the slope of $\beta_C(\epsilon)$, this leads to either an over- or underestimation of ϵ^* .

Finally, we can compare the ranges for the largest considered system size of 5×5 (cf. right panel of Fig. 7). In contrast to the smaller lattices, the difference between the torus and Klein bottle in terms becomes smaller with increasing lattice size. One possible explanation is that the boundary effects should become less pronounced as the system grows. The bulk of the system scales quicker than the boundary. Due to run time considerations, the data for the Klein bottle are not averaged over 10 independent runs. It represents the analysis of a randomly chosen dimer for each class. Due to the large number of 1096 different dimer classes, we aimed to limit the computational time.

In an experimental setting, a configuration with as little fine-tuning of ϵ is desirable. Dimer coverings with the largest violation range are most interesting, instead of the extremal cases for a given model. In the considered systems, the configurations with maximal violation always coincide with the configuration on the upper bound of the ϵ^* range (cf. Fig. 7).

These configurations are potential candidates for experimental realization. Due to the large violation range, it is unnecessary to fine-tune the coupling. The large gap between the classical and quantum values allows for an on-device energy minimization with variational methods, such as variational quantum eigensolvers [50,51].

VI. CONCLUSIONS AND OUTLOOK

Despite the immense complexity of studying Bell non-locality in many-body systems, the exploration of Bell nonlocality in terms of nearest-neighbor dimer Hamiltonians is an accessible avenue.

We find the violation regions for a host of two-dimensional CHSH inequalities by optimizing the coupling of a dimer Hamiltonian. The intersections of the classical bound and the quantum value signify the boundaries of the violation interval. The larger the interval, the larger the Bell inequality's capacity to indicate nonlocality. Both the classical bound and the quantum value are evaluated numerically with tensor methods. For the classical bound, we use tropical tensor networks, while the quantum value is evaluated as the ground state of a DMRG computation.

Dimer coverings with maximal violation region are interesting candidates for experimental realizations. The considered system sizes are well within reach and the coupling scheme in terms of dimers is practically realizable. Furthermore, the inequalities could be tailored to the quality of individual links of, for instance, a superconducting device. Links with coupling problems could be given a low weight, while the rest of the lattice is still optimized for the best dimer covering. The optimization of boundary conditions and coupling configuration (in terms of dimer covering) gives a practical approach, with the same resources, to better certify the nonlocality generation capabilities of existing quantum processors.

Looking ahead, there are several possible improvements to our approach. The used numerical methods could be optimized by incorporating further symmetries of the Hamiltonian. This is possible for both exact diagonalization and MPS computations. Since the system is two dimensional, projected entangled pair states (PEPSs) is another option to compute at least a variationally constrained quantum value [52,53]. Due to the iterative procedure when finding the boundaries of the violating interval, it will be important to choose the algorithms for computing the quantum value and classical bound with their runtime in mind.

The investigation of the square lattice is a choice. Since superconducting devices are often based on heavy-hexagon [54] or honeycomb [55] lattices, our approach could be naturally extended to nonsquare lattices, possibly with trimer interactions [56].

The code to generate the data used in this paper is available online; see Ref. [57]. The actual data used in this manuscript are available in Ref. [58].

ACKNOWLEDGMENTS

The authors acknowledge fruitful discussions with Weikang Li. P.E. and J.T. acknowledge the support re-

ceived by the Dutch National Growth Fund (NGF), as part of the Quantum Delta NL program. P.E. additionally acknowledges the support received through the NWO-Quantum Technology program (Grant No. NGF.1623.23.006). J.T. acknowledges the support received from the European Union's Horizon Europe research and innovation programme through the ERC StG FINE-TEA-SQUAD (Grant No. 101040729). This publication is part of the "Quantum Inspire - the Dutch Quantum Computer in the Cloud" project (with Project No. NWA.1292.19.194) of the NWA research program "Research on Routes by Consortia (ORC)," which is funded by the Netherlands Organization for Scientific Research (NWO). A.A. acknowledges support from the Austrian Science Fund (FWF) (Projects No. P 33730-N and No. 10.55776/PAT2839723) and by the ESQ Discovery program (Erwin Schrödinger Center for Quantum Science & Technology), hosted by the Austrian Academy of Sciences (ÖAW). Parts of this work were performed by using the compute resources from the Academic Leiden Interdisciplinary Cluster Environment (ALICE) provided by Leiden University.

The views and opinions expressed here are solely those of the authors and do not necessarily reflect those of the funding institutions. Neither of the funding institutions can be held responsible for them.

APPENDIX A: CONNECTION FROM HAMILTONIANS TO BELL INEQUALITIES

Here we show how to construct the multipartite Bell inequality with m inputs and two outcomes on a square $n \times n$ 2D dimer coverings. Then, conversely, for a given quantum spin Hamiltonian, we explain how to find the Bell inequality such that its Bell operator coincides with this Hamiltonian.

To construct the multipartite Bell inequality of m inputs and two outcomes on square $n \times n$ 2D lattices, we pick a dimer covering of the lattice first, then place a higher weight on the links within the dimer. Then, given a dimer covering, one can construct its corresponding multipartite Bell inequality,

$$I(\epsilon) := \sum_{\langle i,j \rangle} f_{i,j}(\epsilon) \cdot \mathcal{I}_{2,m,2}^{(i,j)}, \tag{A1}$$

where $f_{i,j}(\epsilon)$ is as defined in Eq. (13) and $\mathcal{I}_{2,m,2}^{(i,j)}$ denotes the bipartite Bell expression between nodes i and j. One can see that for each link between node i and j of the dimer, we assign a $\mathcal{I}_{2,m,2}^{(i,j)}$ with higher weight $(1+\epsilon)\mathcal{I}^{(i,j)}$ associated to it. Similarly, we assign $(1-\epsilon)\mathcal{I}^{(i,j)}$ for the two adjacent nodes i and j that are not linked.

Now, we illustrate the procedure for deriving Bell expressions corresponding to a given Hamiltonian of the form

$$H = \sum_{\langle i,j \rangle} f_{i,j}(\epsilon) H_2, \tag{A2}$$

where

$$H_{2} = m \left(\cos^{2} \frac{\pi}{2m} \sigma_{x}^{(i)} \sigma_{x}^{(j)} + \cos \frac{\pi}{2m} \sin \frac{\pi}{2m} \sigma_{x}^{(i)} \sigma_{z}^{(j)} \right. \\ \left. + \sin \frac{\pi}{2m} \cos \frac{\pi}{2m} \sigma_{z}^{(i)} \sigma_{x}^{(j)} - \cos^{2} \frac{\pi}{2m} \sigma_{z}^{(i)} \sigma_{z}^{(j)} \right),$$

and $f_{i,j}(\epsilon)$ is defined as in Eq. (13). Note that this Hamiltonian H is a particular case of the Bell inequality $I(\epsilon)$ in (A1) when

 $\mathcal{I}_{2,m,2}^{(i,j)}$ is the chained Bell inequality [22,59]. Our goal is to find a Bell operator \mathcal{B} that corresponds to the given Hamiltonian H in Eq. (A2) such that $\mathcal{B} \equiv H$. If we restrict to the local part of the Hamiltonian, then the structure of H_2 requires a specific Bell scenario: the number of parties in local parts is two because of the tensor form of H_2 , and the number of outcomes, d=2, is due to the local dimension of the Pauli matrices. Thus, for the local part H_2 , we only need to consider the Bell scenario (2, m, 2). To have nontrivial correlations, we set $m \geqslant 2$. According to the general form of the Bell expression in (2, m, 2), the associated Bell operator can be written as

$$\mathcal{B}_2 = \sum_{x_1, x_2 = 0}^{m-1} \sum_{k_1, k_2 = 0}^{1} \alpha_{x_1, x_2}^{(k_1, k_2)} A_{1, x_1}^{(k_1)} A_{2, x_2}^{(k_2)}, \tag{A3}$$

where $A_{i,x_i}^{(k_i)} = \sum_{a_i=0}^1 (-1)^{a_i k_i} F_{x_i,a_i}$ is the discrete Fourier transform of a positive operator-valued measure (POVM) $\{F_{x_i,a_i}\}_{a_i=0}^1$ representing the measurement on the ith party in the basis x_i . Note that $[A_{1,x_1}^{(k_1)}, A_{2,x_2}^{(k_2)}] = 0$ for $x_1, x_2 \in [m]$, $k_1, k_2 \in \{0, 1\}$.

Our goal is to find operators $A_{1,x_1}^{(k_1)}$, $A_{2,x_2}^{(k_2)}$ and coefficients $\alpha_{x_1,x_2}^{(k_1,k_2)}$ that give rise to a nontrivial Bell inequality. Due to the expression of the Hamiltonian H in Eq. (A2), we assume that

$$A_{1,x_1}^{(k_1)} = \cos \theta_{x_1}^{(k_1)} \sigma_x + \sin \theta_{x_1}^{(k_1)} \sigma_z,$$

$$A_{2,x_2}^{(k_2)} = \cos \phi_{x_2}^{(k_2)} \sigma_x + \sin \phi_{x_2}^{(k_2)} \sigma_z,$$
(A4)

where $x_1, x_2 \in [m]$, $k_1, k_2 \in \{0, 1\}$. As we will see in the example below in (A9), by choosing $A_{1,x_1}^{(k_1)}$ and $A_{2,x_2}^{(k_2)}$ in this way, the matrix T will have a desirable form. Then, the general form of the Bell operator can be written as

$$\mathcal{B}_{2} = \sum_{x_{1}, x_{2}=0}^{m-1} \sum_{k_{1}, k_{2}=0}^{1} \alpha_{x_{1}, x_{2}}^{(k_{1}, k_{2})} \cdot \left(\cos \theta_{x_{1}}^{(k_{1})} \sigma_{x} + \sin \theta_{x_{1}}^{(k_{1})} \sigma_{z}\right)$$

$$\otimes \left(\cos \phi_{x_{2}}^{(k_{2})} \sigma_{x} + \sin \phi_{x_{2}}^{(k_{2})} \sigma_{z}\right). \tag{A5}$$

Next, to find the coefficients $\alpha_{x_1,x_2}^{(k_1,k_2)}$ of the Bell expression, we write the above Bell operator as a system of linear equations by projecting into the basis $\{\sigma_x \otimes \sigma_x, \sigma_x \otimes \sigma_z, \sigma_z \otimes \sigma_x, \sigma_z \otimes \sigma_z\}$. And the projection of H_2 is given by $\text{Tr}[(\sigma_i \otimes \sigma_j)H_2], i, j \in \{x, z\}$. In this way, we have

$$T \cdot \vec{\alpha} = \vec{b},$$
 (A6)

where

$$T = \begin{pmatrix} \cos\theta_0^{(0)}\cos\phi_0^{(0)} & \dots & \cos\theta_{x_1}^{(k_1)}\cos\phi_{x_2}^{(k_2)} & \dots \\ \cos\theta_0^{(0)}\sin\phi_0^{(0)} & \dots & \cos\theta_{x_1}^{(k_1)}\sin\phi_{x_2}^{(k_2)} & \dots \\ \sin\theta_0^{(0)}\cos\phi_0^{(0)} & \dots & \sin\theta_{x_1}^{(k_1)}\cos\phi_{x_2}^{(k_2)} & \dots \\ \sin\theta_0^{(0)}\sin\phi_0^{(0)} & \dots & \sin\theta_{x_1}^{(k_1)}\sin\phi_{x_2}^{(k_2)} & \dots \end{pmatrix}$$

is a $4 \times 4m^2$ matrix, $\vec{\alpha} = (\alpha_{0,0}^{0,0}, \dots, \alpha_{x_1,x_2}^{(k_1,k_2)}, \dots, \alpha_{m-1,m-1}^{(1,1)})^T$,

$$\vec{b} = \{ \text{Tr}[(\sigma_x \otimes \sigma_x) H_2], \text{Tr}[(\sigma_x \otimes \sigma_z) H_2], \text{Tr}[(\sigma_z \otimes \sigma_x) H_2],$$
$$\text{Tr}[(\sigma_z \otimes \sigma_z) H_2] \}^T,$$

$$=2m\left(2\cos^2\frac{\pi}{2m},\sin\frac{\pi}{m},\sin\frac{\pi}{m},-2\cos^2\frac{\pi}{2m}\right)^T.$$
 (A7)

Assume that we fix $\theta_{x_1}^{(k_1)}$, $\phi_{x_2}^{(k_2)}$ for $x_1, x_2 \in [m]$, $k_1, k_2 \in \{0, 1\}$; then we can write the matrix T. Note that in our case, we need to consider the boundary conditions of the dimer coverings, so we assume $A_i = B_i$, which implies $\theta_{x_1}^{(k_1)} = \phi_{x_2}^{(k_2)}$. This ensures that the measurements of the site on the boundary are consistent. Since rank $(T) \leq \min\{4, 4m^2\}$, we have the following two cases: If T is invertible [m = 2 and rank(T) = 4], there is a unique solution for $\vec{\alpha} = T^{-1}\vec{b}$. Thus there is a unique Bell expression corresponding to H with operators given by Eq. (A5). If T is not invertible, there exists a family of solutions for $\vec{\alpha}$. It means there are multiple Bell expressions corresponding to H with operators given by Eq. (A5).

After obtaining the Bell expression $\mathcal{I}_{2,m,2}$ corresponding to the Bell operator in Eq. (A5), one can construct the Bell expression corresponding to H in Eq. (A2) as follows:

$$I(\epsilon) = \sum_{\langle i,j \rangle} f_{i,j} \cdot \mathcal{I}_{2,m,2}^{(i,j)},\tag{A8}$$

where $f_{i,j}(\epsilon)$ is defined as in Eq. (13) and i, j label the parties. Finally, as an illustrative example, we show how to find the associated operator of the CHSH inequality from the Hamiltonian in Eq. (A2) when m=2. First, we assume that $\theta_0=$ $\phi_0 = 0$, $\theta_1 = \phi_1 = \pi/2$; then the operators are $A_0 = B_0 = \sigma_x$, $A_1 = B_1 = \sigma_z$. The Bell operator of the (2,2,2) scenario without local operators is $\sum_{x,y=0,1} \alpha_{x,y} A_x B_y$, which can be written as a system of linear equations by projecting into the basis $\{\sigma_i \otimes \sigma_i\}$, and the projection of $H_2 = (\sigma_x \sigma_x + \sigma_x \sigma_z + \sigma_z \sigma_x - \sigma_z \sigma_x)$ $\sigma_z \sigma_z$) is given by Tr[$(\sigma_i \otimes \sigma_i)H_2$], $i, j \in \{x, z\}$. Then we have

$$T \cdot \vec{\alpha} = \vec{b},\tag{A9}$$

where

$$T = \begin{pmatrix} 1 & 0 & 0 & 0 \\ 0 & 1 & 0 & 0 \\ 0 & 0 & 1 & 0 \\ 0 & 0 & 0 & 1 \end{pmatrix},$$

and $\vec{\alpha} = (\alpha_{0,0}, \alpha_{0,1}, \alpha_{1,0}, \alpha_{1,1})^T$, $\vec{b} = (4, 4, 4, -4)^T$. Then one can obtain $\vec{\alpha} = T^{-1} \cdot \vec{b} = (4, 4, 4, -4)^T$. The associated Bell expression is $\mathcal{I}^{(i,j)} = 4(A_0B_0 + A_0B_1 + A_1B_0 - A_1B_1)$. Finally, since $A_i, B_i \in \{-1, 1\}, i, j \in \{0, 1\}$, one obtains $\mathcal{I}^{(i,j)} \geqslant$ -8, which is the (scaled) CHSH inequality. In this case, the Bell inequality associated with the Hamiltonian H in Eq. (14) is

$$I(\epsilon) = 4 \sum_{\langle i,j \rangle} f_{i,j} \mathcal{I}^{(i,j)}, \tag{A10}$$

where $\mathcal{I}^{(i,j)} = (A_0^{(i)}A_0^{(j)} + A_0^{(i)}A_1^{(j)} + A_1^{(i)}A_0^{(j)} - A_1^{(i)}A_1^{(j)}),$ $f_{i,j}(\epsilon)$ is defined as in Eq. (13), and i,j label the parties.

APPENDIX B: MATHEMATICAL BACKGROUND FOR THE CLASSIFICATION OF DIMER CONFIGURATIONS

In two spatial dimensions, the amount of possible dimer configurations increases dramatically with the number of sites. However, some dimer configurations on the twodimensional square lattice with fixed boundary conditions are related by symmetries. This allows us to group them into a single class. Subsequently, we only need to investigate a representative 2D square dimer covering from each class, which allows us to reduce computational time.

Let $S_n = \{S^{(1)}, S^{(2)}, \dots, S^{(k)}, \dots\}$ be a finite set of 2D square dimer coverings $(n \times n \text{ nodes})$ with boundary conditions, and let G be a group with identity element e. Then, a left action on \mathbb{S}_n is a map $G \times \mathbb{S}_n \to \mathbb{S}_n$, written $(g, S^{(k)}) \mapsto$ $g \cdot S^{(k)}$, such that

$$g_1 \cdot (g_2 \cdot S^{(k)}) = (g_1 \cdot g_2) \cdot S^{(k)}$$
 (B1)

and $e \cdot S^{(k)} = S^{(k)}$ for all $g_1, g_2 \in G$ and $S^{(k)} \in \mathbb{S}_n$. Let $\mathbb{S}_{n,T} = \{S_T^{(1)}, S_T^{(2)}, \dots, S_T^{(k)}, \dots\}$ be a finite set of 2D square lattice $(n \times n \text{ nodes})$ of torus (the boundary $aba^{-1}b^{-1}$). For $S_T^{(k)} \in \mathbb{S}_{n,T}$, we can obtain its equivalent dimer coverings with the same boundary conditions, $S_T^{(k)'}$, if some of the following operations are applied:

(1) Right shift O_{rs} . The operation right shift is a bijection O_{rs} from the set $\mathbb{S}_{n,T}$ to the set $\mathbb{S}_{n,T}$ as follows:

$$O_{\text{rs}}: \mathbb{S}_{n,T} \to \mathbb{S}_{n,T},$$

 $S_T^{(k)} := (\mathbf{a}_0, \mathbf{a}_1, \dots, \mathbf{a}_{n-1}) \mapsto (\mathbf{a}_1, \dots, \mathbf{a}_{n-1}, \mathbf{a}_0),$
(B2)

where \mathbf{a}_i is the *i*th column with *n* nodes of $S_T^{(k)}$, and i = $0, \ldots, n-1.$

(2) Up shift O_{us} . The operation up shift O_{us} is defined as

$$O_{us}: \mathbb{S}_{n,T} \to \mathbb{S}_{n,T}$$
,

$$S_T^{(k)} := \begin{pmatrix} \mathbf{b}_0 \\ \vdots \\ \mathbf{b}_{n-2} \\ \mathbf{b}_{n-1} \end{pmatrix} \mapsto \begin{pmatrix} \mathbf{b}_{n-1} \\ \mathbf{b}_0 \\ \vdots \\ \mathbf{b}_{n-2} \end{pmatrix}, \tag{B3}$$

where \mathbf{b}_i is the jth row with n nodes of $S_T^{(k)}$ and j = $0, \ldots, n-1.$

(3) Vertically mirrored $O_{\rm vm}$. The operation vertical mirror is a bijection O_{vm} from the set $S_{n,T}$ to the set $S_{n,T}$ as follows:

$$O_{\text{vm}}: \mathbb{S}_{n,T} \to \mathbb{S}_{n,T},$$

 $S_T^{(k)} := (\mathbf{a}_0, \mathbf{a}_1, \dots, \mathbf{a}_{n-1}) \mapsto (\mathbf{a}_{n-1}, \dots, \mathbf{a}_1, \mathbf{a}_0),$ (B4)

where \mathbf{a}_i is the *i*th column with *n* nodes of $S_T^{(k)}$, and i = $0, \ldots, n-1$.

(4) Horizontally mirrored $O_{\rm hm}$. The operation horizontal mirror O_{hm} is

$$S_{T}^{(k)} := \begin{pmatrix} \mathbf{b}_{0} \\ \vdots \\ \mathbf{b}_{n-2} \\ \mathbf{b}_{n-1} \end{pmatrix} \mapsto \begin{pmatrix} \mathbf{b}_{n-1} \\ \mathbf{b}_{n-2} \\ \vdots \\ \mathbf{b}_{0} \end{pmatrix}, \tag{B5}$$

where \mathbf{b}_j is the jth row with n nodes of $S_T^{(k)}$ and j = $0, \ldots, n-1.$

(5) Rotation O_r . The operation rotation can be written as

$$O_{\mathbf{r}}: \mathbb{S}_{n,T} \to \mathbb{S}_{n,T},$$
 (B6)

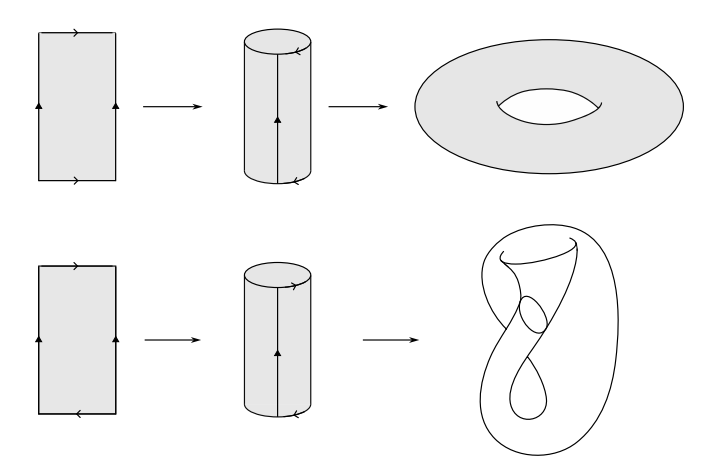


FIG. 9. Sketch of the topology of a torus (top) and a Klein bottle (bottom). The arrows, from left to right, indicate the successive merging of boundaries.

$$S_T^{(k)} := (\mathbf{a}_0, \mathbf{a}_1, \dots, \mathbf{a}_{n-1})^T \mapsto \begin{pmatrix} \bar{\mathbf{a}}_0^T \\ \bar{\mathbf{a}}_1^T \\ \vdots \\ \bar{\mathbf{a}}_{n-1}^T \end{pmatrix}, \tag{B7}$$

where \mathbf{a}_i is the *i*th column with *n* nodes of $S_T^{(k)}$, $\bar{\mathbf{a}}_i^T$ is the transpose after reversing the order of the elements along the length of the vector \mathbf{a}_i , and $i = 0, \dots, n-1$. For example, if $\mathbf{a}_0 = (2, 1, 0)^T$, then $\bar{\mathbf{a}}_0 = (0, 1, 2)^T$ and $\bar{\mathbf{a}}_0^T = (0, 1, 2)$.

One can check that for the nonempty set of 2D dimer coverings $\mathbb{S}_{n,T}$ of torus (the boundary $aba^{-1}b^{-1}$) depicted in Fig. 9, the group acting on $\mathbb{S}_{n,T}$ is

$$G_{T} = \langle O_{rs}, O_{us}, O_{vm}, O_{hm}, O_{r} :$$

$$(O_{rs})^{n} = (O_{us})^{n} = (O_{vm})^{2} = (O_{hm})^{2} = (O_{r})^{4} = e,$$

$$O_{vm}O_{rs} = (O_{rs})^{-1}O_{vm}, O_{hm}O_{us} = (O_{us})^{-1}O_{hm},$$

$$O_{vm}O_{r} = (O_{r})^{-1}O_{vm}, O_{hm}O_{r} = (O_{r})^{-1}O_{hm} \rangle.$$
(B8)

Similarly, let $\mathbb{S}_{n,KB} = \{S_{KB}^{(1)}, S_{KB}^{(2)}, \dots, S_{KB}^{(k)}, \dots\}$ be a finite set of 2D dimer coverings $(n \times n \text{ nodes})$ of Klein bottle (the boundary $aba^{-1}b$) as shown in Fig. 9. For $S_{KB}^{(k)} \in \mathbb{S}_{n,KB}$, we can obtain its equivalent dimer coverings with the same boundary conditions, $S_{KB}^{(k)}$, if some of the following operations are applied:

(1) Right shift O'_{rs} . The operation right shift is a bijection O'_{rs} from the set $\mathbb{S}_{n,KB}$ to the set $\mathbb{S}_{n,KB}$ as follows:

$$O'_{rs}: \mathbb{S}_{n,KB} \to \mathbb{S}_{n,KB},$$

 $S^{(k)}_{KB} := (\mathbf{a}_0, \mathbf{a}_1, \dots, \mathbf{a}_{n-1}) \mapsto (\mathbf{a}_1, \dots, \mathbf{a}_{n-1}, \bar{\mathbf{a}}_0),$
(B9)

where \mathbf{a}_i is the *i*th column with *n* nodes of $S_{KB}^{(k)}$, $\bar{\mathbf{a}}_i$ reverses the order of the elements along the length of the vector \mathbf{a}_i , and $i = 0, \dots, n-1$.

(2) Vertically mirrored O'_{vm} . The operation vertical mirror is a bijection O'_{vm} from the set $\mathbb{S}_{n,KB}$ to the set $\mathbb{S}_{n,KB}$ as

TABLE I. Number of group orbits, i.e., different classes of dimer configurations. In parentheses are given the minimal and the maximal number of dimer configurations in a class, respectively.

Size/Boundary	Torus	Klein bottle
3 × 3	3 (18,36)	11 (3,12)
4×4	13 (4,64)	36 (1,16)
5×5	113 (50,200)	1096 (5,20)

follows:

$$O'_{\text{vm}}: \mathbb{S}_{n,KB} \to \mathbb{S}_{n,KB},$$

$$S_{KB}^{(k)} := (\mathbf{a}_0, \mathbf{a}_1, \dots, \mathbf{a}_{n-1}) \mapsto (\bar{\mathbf{a}}_0, \mathbf{a}_{n-1}, \dots, \mathbf{a}_1),$$
(B10)

where \mathbf{a}_i is the *i*th column of $S_{KB}^{(k)}$ and $\bar{\mathbf{a}}_i$ reverses the order of the elements along the length of the vector \mathbf{a}_i , $i = 0, \ldots, n-1$.

Then we can obtain that for the set $S_{n,KB}$, the group acting on it is

$$G_{KB} = \langle O'_{rs}, O'_{vm} : (O'_{rs})^{2n} (O'_{vm})^2 = e,$$

 $O'_{vm} O'_{rs} = (O'_{rs})^{-1} O'_{vm} \rangle.$ (B11)

APPENDIX C: DIMER CLASSIFICATION

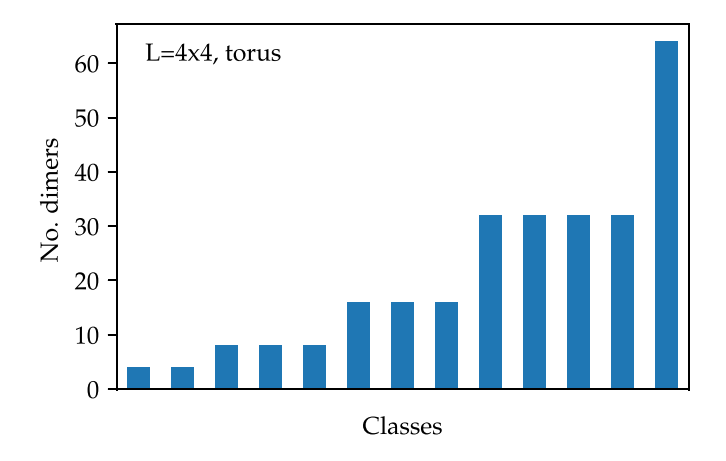
Given the symmetries describe in Appendix B, multiple dimer configurations lead to the same classical bounds and quantum values. By considering only a single representative of each class, the amount of dimer configurations drops from 19 600 individual dimers to 113 representatives.

As a classification procedure, we choose a depth-first search. Each dimer configuration is considered as a vertex of a graph. Two vertices of the graph are connected by an edge if there exists a symmetry operation of the lattice transforming one dimer covering into the other. To classify the dimers, we do not need to construct this graph explicitly, we only have to explore its connected components. Each connected component corresponds to one distinct group orbit, i.e., a class of dimer coverings. We start the classification procedure by choosing an arbitrary dimer configuration, i.e., an arbitrary vertex in the graph. Following the spirit of a depth-first search, we apply a symmetry operation of the lattice recursively to reach new vertices. If a vertex has not been visited before, we mark it and apply a symmetry operation to the new vertex. If it has been marked before, we perform no operation to exit the recursion.

Once the recursion terminates, all marked vertices belong to the same class. We repeat the procedure until all vertices have been marked with a class label.

The number of classes varies depending on the different system sizes. An overview of the amount of dimer classes as well as the minimal and maximal number of representatives in each class is given Table I.

Figure 10 shows the distribution of the dimer coverings over the different classes in more detail for periodic and Klein bottle boundary conditions in a system of size 4×4 . Since the numbering of the classes is arbitrary, the labels on the horizontal axis are left blank. Here, the classes are ordered by number of dimer coverings for readability.



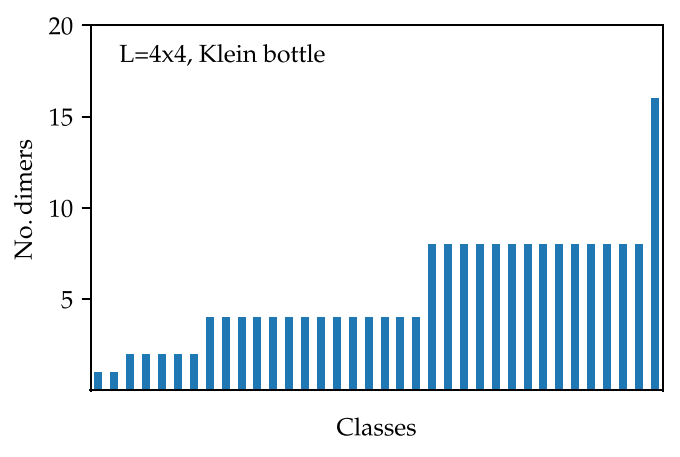


FIG. 10. Statistics of the dimer configurations. Top: Statistics for a system on a torus of size 4×4 . Bottom: Statistics for a system on a Klein bottle of the same size.

APPENDIX D: EXAMPLE TROPICAL OPTIMIZATION

An example for an optimization problem is to find the shortest path in a directed graph in k steps. The directed graph G=(V,E) is a tuple consisting of a set of vertices V and a set of weighted, directed edges E=(u,v,w), where $u,v\in V$ and $w\in \mathbb{R}\cup \{+\infty\}$ is the weight of the edge from vertex u to v. If there exists no edge from u to v, we set $w=+\infty$.

The graph can be equivalently represented by a $|V| \times |V|$ adjacency matrix W. Each entry W_{uv} of the matrix corresponds to the weight of the directed edge (u, v). This adjacency matrix is the input to the tropical optimization procedure.

The goal of the optimization is to find the shortest path in the graph from vertex u to vertex v in k steps. Here, "shortest"

means the minimal amount of accumulated weight. While this problem is a classical application for Dijkstra's algorithm, it can be formulated as tropical matrix multiplication. The (u, v) entry of the matrix $W^{\odot k}$ is the length of the shortest path in k steps from vertex u to v in the directed graph G. Here, $W^{\odot k}$ is the tropical matrix power, i.e., applying tropical matrix multiplication k times. More concretely, we compute the tropical matrix product as

$$(A \odot B)_{ij} = \bigoplus_{l} A_{il} \odot B_{lj}$$

$$= \min_{l} (A_{il} + B_{lj}).$$
(D1)

In the third line, the relation to a minimization task becomes evident. The tropical matrix multiplication selects the minimum weight from all possible edges connecting the vertices i and j.

As an example, let us consider the adjacency matrix

$$W = \begin{pmatrix} 1 & 2 & +\infty \\ +\infty & 3 & 4 \\ 5 & 6 & 1 \end{pmatrix}.$$
 (D2)

To obtain the shortest path in two steps, we compute

$$W^{\odot 2} = \begin{pmatrix} 2 & 3 & 6 \\ 9 & 6 & 5 \\ 6 & 7 & 2 \end{pmatrix}. \tag{D3}$$

The shortest path from the vertex 1 to 2 in two steps on graph G is 3, which corresponds to the entry $W_{1,2}^{\odot 2}$.

Additionally, the shortest closed path in k steps can be obtained with the tropical trace, tropTrace($W^{\odot k}$). The tropical trace corresponds to taking the minimal diagonal entry of a matrix. In our example, the minimum closed path in two steps is 2, which is tropTrace($W^{\odot 2}$).

APPENDIX E: PARAMETERS FOR NUMERICAL SIMULATIONS

The MPS simulations for the quantum were performed with the TeNPy Library (version 0.10.0) [60]. The MPS simulations are performed with a virtual bond dimension of D=300. Since the ground-state search is called repeatedly during the optimization, this bond dimension is a good compromise between accuracy and solution time. The ground state is considered to be converged if the energy does not change more than 10^{-4} or the entropy does not change more than 10^{-3} .

In the Brent-Dekker algorithm, the root is considered to be converged if it does not change more than 10^{-3} .

^[1] J. S. Bell, On the Einstein-Podolsky-Rosen paradox, Phys. Phys. Fiz. 1, 195 (1964).

^[2] A. Fine, Hidden variables, joint probability, and the Bell inequalities, Phys. Rev. Lett. **48**, 291 (1982).

^[3] N. Brunner, D. Cavalcanti, S. Pironio, V. Scarani, and S. Wehner, Bell nonlocality, Rev. Mod. Phys. 86, 419 (2014).

^[4] B. Hensen, H. Bernien, A. E. Dréau, A. Reiserer, N. Kalb, M. S. Blok, J. Ruitenberg, R. F. L. Vermeulen, R. N. Schouten, C. Abellán, W. Amaya, V. Pruneri, M. W. Mitchell, M. Markham,

D. J. Twitchen, D. Elkouss, S. Wehner, T. H. Taminiau, and R. Hanson, Loophole-free Bell inequality violation using electron spins separated by 1.3 kilometres, Nature (London) **526**, 682 (2015).

^[5] M. Giustina, M. A. M. Versteegh, S. Wengerowsky, J. Handsteiner, A. Hochrainer, K. Phelan, F. Steinlechner, J. Kofler, J.-Å. Larsson, C. Abellán, W. Amaya, V. Pruneri, M. W. Mitchell, J. Beyer, T. Gerrits, A. E. Lita, L. K. Shalm, S. W. Nam, T. Scheidl, R. Ursin *et al.*, Significant-loophole-free test

- of Bell's theorem with entangled photons, Phys. Rev. Lett. 115, 250401 (2015).
- [6] L. K. Shalm, E. Meyer-Scott, B. G. Christensen, P. Bierhorst, M. A. Wayne, M. J. Stevens, T. Gerrits, S. Glancy, D. R. Hamel, M. S. Allman, K. J. Coakley, S. D. Dyer, C. Hodge, A. E. Lita, V. B. Verma, C. Lambrocco, E. Tortorici, A. L. Migdall, Y. Zhang, D. R. Kumor *et al.*, Strong loophole-free test of local realism, Phys. Rev. Lett. 115, 250402 (2015).
- [7] W. Rosenfeld, D. Burchardt, R. Garthoff, K. Redeker, N. Ortegel, M. Rau, and H. Weinfurter, Event-ready Bell test using entangled atoms simultaneously closing detection and locality loopholes, Phys. Rev. Lett. 119, 010402 (2017).
- [8] S. Storz, J. Schär, A. Kulikov, P. Magnard, P. Kurpiers, J. Lütolf, T. Walter, A. Copetudo, K. Reuer, A. Akin, J.-C. Besse, M. Gabureac, G. J. Norris, A. Rosario, F. Martin, J. Martinez, W. Amaya, M. W. Mitchell, C. Abellan, J.-D. Bancal *et al.*, Loophole-free Bell inequality violation with superconducting circuits, Nature (London) 617, 265 (2023).
- [9] A. Acín, N. Brunner, N. Gisin, S. Massar, S. Pironio, and V. Scarani, Device-independent security of quantum cryptography against collective attacks, Phys. Rev. Lett. 98, 230501 (2007).
- [10] S. Pironio, Ll. Masanes, A. Leverrier, and A. Acín, Security of device-independent quantum key distribution in the boundedquantum-storage model, Phys. Rev. X 3, 031007 (2013).
- [11] R. Colbeck and R. Renner, Free randomness can be amplified, Nat. Phys. 8, 450 (2012).
- [12] R. Gallego, L. Masanes, G. De La Torre, C. Dhara, L. Aolita, and A. Acín, Full randomness from arbitrarily deterministic events, Nat. Commun. 4, 2654 (2013).
- [13] I. Šupić, R. Augusiak, A. Salavrakos, and A. Acín, Self-testing protocols based on the chained Bell inequalities, New J. Phys. 18, 035013 (2016).
- [14] D. Rosset, J.-D. Bancal, and N. Gisin, Classifying 50 years of Bell inequalities, J. Phys. A: Math. Theor. 47, 424022 (2014).
- [15] J. F. Clauser, M. A. Horne, A. Shimony, and R. A. Holt, Proposed experiment to test local hidden-variable theories, Phys. Rev. Lett. 23, 880 (1969).
- [16] D. Collins, N. Gisin, N. Linden, S. Massar, and S. Popescu, Bell inequalities for arbitrarily high-dimensional systems, Phys. Rev. Lett. 88, 040404 (2002).
- [17] Ll. Masanes, Tight Bell inequality for d-outcome measurements correlations, Quantum Inf. Comput. 3, 345 (2003).
- [18] B. Chazelle, An optimal convex hull algorithm in any fixed dimension, Discrete Comput. Geom. 10, 377 (1993).
- [19] F. Baccari, D. Cavalcanti, P. Wittek, and A. Acín, Efficient device-independent entanglement detection for multipartite systems, Phys. Rev. X 7, 021042 (2017).
- [20] R. Schmied, J.-D. Bancal, B. Allard, M. Fadel, V. Scarani, P. Treutlein, and N. Sangouard, Bell correlations in a Bose-Einstein condensate, Science 352, 441 (2016).
- [21] N. J. Engelsen, R. Krishnakumar, O. Hosten, and M. A. Kasevich, Bell correlations in spin-squeezed states of 500 000 atoms, Phys. Rev. Lett. 118, 140401 (2017).
- [22] J. Tura, G. De las Cuevas, R. Augusiak, M. Lewenstein, A. Acín, and J. I. Cirac, Energy as a detector of nonlocality of many-body spin systems, Phys. Rev. X 7, 021005 (2017).
- [23] Z. Wang, S. Singh, and M. Navascués, Entanglement and non-locality in infinite 1D systems, Phys. Rev. Lett. 118, 230401 (2017).

- [24] J. Tura, A. B. Sainz, T. Vértesi, A. Acín, M. Lewenstein, and R. Augusiak, Translationally invariant multipartite Bell inequalities involving only two-body correlators, J. Phys. A: Math. Theor. 47, 424024 (2014).
- [25] M. Hu and J. Tura, Tropical contraction of tensor networks as a Bell inequality optimization toolset, arXiv:2208.02798.
- [26] B. S. Cirel'son, Quantum generalizations of Bell's inequality, Lett. Math. Phys. 4, 93 (1980).
- [27] S. Popescu and D. Rohrlich, Quantum nonlocality as an axiom, Found. Phys. 24, 379 (1994).
- [28] J. Tura, R. Augusiak, A. B. Sainz, T. Vértesi, M. Lewenstein, and A. Acín, Detecting nonlocality in many-body quantum states, Science 344, 1256 (2014).
- [29] J. Tura, R. Augusiak, A. B. Sainz, B. Lücke, C. Klempt, M. Lewenstein, and A. Acín, Nonlocality in many-body quantum systems detected with two-body correlators, Ann. Phys. 362, 370 (2015).
- [30] M. Fadel and J. Tura, Bell correlations at finite temperature, Quantum 2, 107 (2018).
- [31] M. Fadel and J. Tura, Bounding the set of classical correlations of a many-body system, Phys. Rev. Lett. **119**, 230402 (2017).
- [32] S. Wagner, R. Schmied, M. Fadel, P. Treutlein, N. Sangouard, and J.-D. Bancal, Bell correlations in a many-body system with finite statistics, Phys. Rev. Lett. **119**, 170403 (2017).
- [33] Z. Wang and M. Navascués, Two-dimensional translationinvariant probability distributions: Approximations, characterizations and no-go theorems, Proc. R. Soc. A 474, 20170822 (2018).
- [34] B. Toner and F. Verstraete, Monogamy of Bell correlations and Tsirelson's bound, arXiv:quant-ph/0611001.
- [35] P. Cieśliński, L. Knips, M. Kowalczyk, W. Laskowski, T. Paterek, T. Vértesi, and H. Weinfurter, Unmasking the polygamous nature of quantum nonlocality, arXiv:2312.04373.
- [36] J. Gallier and D. Xu, The classification theorem for compact surfaces, in *A Guide to the Classification Theorem for Compact Surfaces*, Geometry and Computing, edited by J. Gallier and D. Xu (Springer, Berlin, 2013), pp. 79–103.
- [37] J.-G. Liu, L. Wang, and P. Zhang, Tropical tensor network for ground states of spin glasses, Phys. Rev. Lett. 126, 090506 (2021).
- [38] D. Maclagan and B. Sturmfels, *Introduction to Tropical Geometry* (American Physical Society, Providence, 2021).
- [39] J. I. Cirac, D. Pérez-García, N. Schuch, and F. Verstraete, Matrix product states and projected entangled pair states: Concepts, symmetries, theorems, Rev. Mod. Phys. 93, 045003 (2021).
- [40] S. Ebadi, A. Keesling, M. Cain, T. T. Wang, H. Levine, D. Bluvstein, G. Semeghini, A. Omran, J.-G. Liu, R. Samajdar, X.-Z. Luo, B. Nash, X. Gao, B. Barak, E. Farhi, S. Sachdev, N. Gemelke, L. Zhou, S. Choi, H. Pichler *et al.*, Quantum optimization of maximum independent set using Rydberg atom arrays, Science 376, 1209 (2022).
- [41] N. Schuch, M. M. Wolf, F. Verstraete, and J. I. Cirac, Computational complexity of projected entangled pair states, Phys. Rev. Lett. 98, 140506 (2007).
- [42] N. Schuch and J. I. Cirac, Matrix product state and mean-field solutions for one-dimensional systems can be found efficiently, Phys. Rev. A 82, 012314 (2010).
- [43] D. Aharonov, I. Arad, and S. Irani, An efficient algorithm for approximating 1D ground states, Phys. Rev. A **82**, 012315 (2010).

- [44] M. B. Hastings, An area law for one-dimensional quantum systems, J. Stat. Mech.: Theory Expt. (2007) P08024.
- [45] I. Arad, A. Kitaev, Z. Landau, and U. Vazirani, An area law and sub-exponential algorithm for 1D systems, arXiv:1301.1162.
- [46] S. R. White, Density matrix formulation for quantum renormalization groups, Phys. Rev. Lett. 69, 2863 (1992).
- [47] S. R. White and D. J. Scalapino, Density matrix renormalization group study of the striped phase in the 2D t-J model, Phys. Rev. Lett. **80**, 1272 (1998).
- [48] R. P. Brent, Algorithms for minimization without derivatives, in *Algorithms for Minimization without Derivatives* (Prentice-Hall, Englewood Cliffs, NJ, 1973), Chap. 4.
- [49] T. Dekker, Finding a zero by means of successive linear interpolation, in *Constructive Aspects of the Fundamental Theorem of Algebra*, edited by B. Dejon and P. Henrici (Wiley-Interscience, London, 1969).
- [50] A. Peruzzo, J. McClean, P. Shadbolt, M.-H. Yung, X.-Q. Zhou, P. J. Love, A. Aspuru-Guzik, and J. L. O'Brien, A variational eigenvalue solver on a photonic quantum processor, Nat. Commun. 5, 4213 (2014).
- [51] J. Tilly, H. Chen, S. Cao, D. Picozzi, K. Setia, Y. Li, E. Grant, L. Wossnig, I. Rungger, G. H. Booth, and J. Tennyson, The variational quantum eigensolver: A review of methods and best practices, Phys. Rep. 986, 1 (2022).

- [52] F. Verstraete and J. Cirac, Renormalization algorithms for quantum-many body systems in two and higher dimensions, arXiv:cond-mat/0407066.
- [53] N. Schuch, I. Cirac, and D. Pérez-García, PEPS as ground states: Degeneracy and topology, Ann. Phys. 325, 2153 (2010).
- [54] Y. Kim, A. Eddins, S. Anand, K. X. Wei, E. van den Berg, S. Rosenblatt, H. Nayfeh, Y. Wu, M. Zaletel, K. Temme, and A. Kandala, Evidence for the utility of quantum computing before fault tolerance, Nature (London) 618, 500 (2023).
- [55] S. Xu, Z.-Z. Sun, K. Wang, H. Li, Z. Zhu, H. Dong, J. Deng, X. Zhang, J. Chen, Y. Wu, C. Zhang, F. Jin, X. Zhu, Y. Gao, A. Zhang, N. Wang, Y. Zou, Z. Tan, F. Shen, J. Zhong *et al.*, Non-Abelian braiding of Fibonacci anyons with a superconducting processor, Nat. Phys. (2024), doi:10.1038/s41567-024-02529-6.
- [56] G. Giudice, F. M. Surace, H. Pichler, and G. Giudici, Trimer states with Z 3 topological order in Rydberg atom arrays, Phys. Rev. B **106**, 195155 (2022).
- [57] See https://gitlab.com/patrick.emonts/topo-bell/.
- [58] See https://gitlab.com/patrick.emonts/topo-bell-data.
- [59] S. L. Braunstein and C. M. Caves, Wringing out better Bell inequalities, Ann. Phys. 202, 22 (1990).
- [60] J. Hauschild and F. Pollmann, Efficient numerical simulations with tensor networks: Tensor network python (TeNPy), SciPost Phys. Lect. Notes, 5 (2018).